Investigation of dynamic stall characteristics for flow past an oscillating airfoil at various reduced frequencies by simultaneous PIV and surface pressure measurements

Deepakkumar M. Sharma[1] and Kamal Poddar[2]

[1] TSI Instruments India Private Limited, Bangalore, India
deepak.sharma@tsi.com

[2] Department of Aerospace Engineering, Indian Institute of Technology Kanpur, India

ABSTRACT

Wind tunnel experiments were carried out at low speed aerodynamics lab at IIT Kanpur to investigate dynamic stall characteristics for a flow past an oscillating NACA 0015 airfoil at various reduced frequencies (κ). The NACA airfoil model was design and developed to incorporate simultaneous surface pressure measurement at the mid-span of the airfoil model along the chord and 2D PIV measurements of the flow-field downstream near the Trailing Edge (TE) vicinity of the oscillating airfoil model subjected to the higher reduced frequency κ up to 0.5. The main objective of this work was to critically assess the effect of κ in the unsteady domain from fully develop to partially develop dynamic stall regimes. For a given constant Reynolds number *Re* of 0.2E06, the instantaneous 2D PIV images were captured for an oscillating airfoil at varied κ. These images have been critically assessed to provide qualitative information and flow visualization of the flow field to trace various dynamic stall events which mainly includes the formation, growth and shedding of Dynamic Stall Vortex (DSV) from the TE.

NOMENCLATURE

Symbol	***Description***	***value***	***unit***
LE	Leading Edge	-	-
TE	Trailing Edge	-	-
LSB	Laminar Separation Bubble	-	-
LEV	Leading Edge Vortex	-	-
DSV	Dynamic Stall Vortex	-	-
TEV	Trailing Edge Vortex	-	-
BL	Boundary Layer	-	-
SHM	Simple Harmonic Motion	-	-
Re	Reynolds Number	$\rho U_\infty c/\mu$	-
ρ	Density of air	1.233	kg/m^3
U_∞	Free-stream velocity	-	*m/s*
c	Chord length	-	*m*
μ	Dynamic Viscosity	1.783×10^{-5}	*kg/ms*
ν	Kinematic Viscosity	$\nu = \mu/\rho$	m^2/s
κ	Reduced frequency	$\kappa = \omega c / 2U_\infty$	-
ω	Circular frequency, Angular velocity	$\omega = 2\pi f$	*rad/s*
f	Oscillating frequency	-	*Hz*
α	Angle of attack	-	*degree*
α_{max}	Maximum angle of attack (Peak)	-	*degree*
α_{min}	Minimum angle of attack (valley)	-	*degree*
α_m	Mean angle of attack	-	*degree*
α_{amp}	Amplitude of oscillation	-	*degree*
$\dot{\alpha}$	Pitch rate	-	*degree/s, rad/s*
t	time	-	*s*
x,y	Coordinates of airfoil profile	-	*m*
s	Distance along the surface measured from LE	-	*m*
η	Thickness of airfoil	-	*m*
ϕ	Phase Angle	$\phi = \omega t$	*rad, degree*
P	Pressure	-	*Pa*
τ	Shear Stress	-	*Pa*
u, l	sub-scripts for Upper and Lower surface of airfoil	-	-

C_l	Sectional Lift Coefficient	-	-
C_d	Sectional Drag Coefficient	-	-
C_{dp}	Sectional Pressure Drag Coefficient	-	
C_n	Sectional Normal force Coefficient	-	-
C_a	Sectional Axial force Coefficient	-	-
C_m	Sectional Pitching Moment Coefficient	-	-
X_{cp}	Center of Pressure	-	-
C_P	Pressure Coefficient	$C_P = (P - P_\infty)/q_\infty$	-
P_∞	Free-stream Static Pressure	-	*Pa*
q_∞	Dynamic Pressure	$q_\infty = \frac{1}{2}\rho U_\infty^2$	*Pa*
χ, γ	C_n-C_m Cross-Correlations	-	-
ξ	Normal Force Defect	-	-
ζ	Pitch damping factor	-	-
rms	Root-Mean-Square	-	-
min, max	sub-scripts for Minimum and Maximum	-	-

INTRODUCTION

Dynamic stall phenomena are the results of an airfoil (wing) undergoing ramp or oscillatory motion having a maximum angle of attack greater than the static stall angle. The unsteady flows induced by the dynamic stall phenomena are characterized by massive separation and formation of large-scale vortical structures. The fundamental understanding of the dynamic stall onset is important to the rotary as well as the fixed wing aircraft configurations [1, 2, 3, 4]. Recent interests in exploiting the dynamic vortex lift on super-maneuverable aircraft and other applications such as wind turbine rotors, compressor blades, etc, require a thorough understanding of dynamic stall process before utilizing the potential of these energetic flows. The present era has been a period of exploring new design limits for virtually the whole spectrum of low chord Reynolds number ($10^5 < Re < 10^6$) flight applications meant for military, commercial, and recreational purposes. The design of sub-scale rotors for helicopter dynamics also falls in this regime of Reynolds number. It is evident, however, that the knowledge of the aerodynamics for these applications is far from complete, especially the phenomena associated with the boundary layer behavior in the context of dynamic stall. This has prompted extensive experimental and computational research in all aspects of the low Reynolds number flight, which includes, wind tunnel testing of the airfoils, developing more efficient computational schemes, numerical and analytical modeling of the laminar separation bubble (LSB) and dynamic stall vortex (DSV) [5, 6]. Thus understanding the physics involved in the behavior of the dynamic stall characteristics in this Reynolds number regime would contribute to the various aerodynamic applications.

EXPERIMENTAL METHODOLOGY

Wind tunnel experiments were conducted on an oscillating ($\alpha = 10^\circ + 15^\circ \sin(\omega t)$) NACA-0015 airfoil model, having the chord length of 0.31m spanning the test-section width of 0.305m [7]. The geometric blockage is within 10% for the maximum angle of attack of 25º. The measured free-stream turbulence level in the 2D wind tunnel test section is within 0.15%.As shown in figure 1, the airfoil model was design and develop to incorporate surface pressure measurement at the mid-span of the airfoil model along the chord and PIV measurements of the flow-field downstream near the TE vicinity of the oscillating airfoil model subjected to the higher κ up to 0.5. The main objective of this work was to critically assess the effect of κ in the unsteady domain from fully develop to partially develop dynamic stall regimes. For a given constant *Re* of 0.2E06, the instantaneous PIV images were captured for an oscillating airfoil at varied κ. Other oscillating parameters which may affect the hysteresis behavior such as airfoil geometry, amplitude of oscillation, mean angle of incidence are kept unchanged. These PIV images are critically assessed to provide qualitative information and flow visualization of the flow field to trace various dynamic stall events which mainly includes the formation, growth and shedding of DSV from the TE.

The surface pressure measurements at the mid-span along the chord are done using two piezo-resistive 32-port ESP pressure scanners from PSI, USA having 20 kHz multiplexing frequency and 0.07% of full scale accuracy. Uncertainty in the calculation of the surface pressure coefficient is about 0.1 %. Schematic sketch of pressure port locations on the NACA airfoil model are shown in figure 2. The surface pressure tapings (#60) are unevenly distributed on the upper & lower surfaces such that the pressure taps were more clouded towards the LE as compared to the TE. This helps in precisely capturing the surface flow phenomena and boundary layer characteristics emerging from the LE [8, 9].

PIV measurements were carried out using the TSI's 2D PIV system. Figure 3 demonstrates the instrumentation and measurement chain for 2D-PIV acquisition for a field of View of 550mm x 550mm using 4MP CCD camera. Flow was

seeded with fog generator. TSI Insight 3G software was used for image data acquisition, processing and analysis. TecPlot software was used for the velocity vector field visualizations and plotting.

PIV is a non-intrusive, flow-field measurement technique, by which a velocity field is measured based on sequentially acquired images of illuminated flow-field within known interval of time. Seeding particles are introduced into the fluid medium and these particles follow the fluid motion. Particles are illuminated by a thin sheet of light produced by a laser, and successive images of the illuminated seeding particles are recorded with a camera, from which average in-plane particle displacements are found. Velocity, vorticity, and streamline fields are then readily computed from the particle displacement information. [10, 11, 12, 13]. An error associated with estimation of the displacement of the particles in pixel unit is 0.1 pixels [14] because the Fast Fourier transform (FFT) was applied for correlation analysis. The inherent uncertainty is in the spatial location of the peak in the correlation function. This is widely accepted to be about 1/10 of a pixel, so by looking at the displacements in the PIV images (we can process with no calibration, and the units will be in pixels) we can determine the uncertainty. Displacements of about 10 pixels give an uncertainty of about 1%.

RESULTS AND DISCUSSIONS

Normal force defect, Pitch damping factor & Free-stream velocity fluctuations:

Hysteresis effect & aerodynamic damping at a given Re = 0.2E06 and the κ varied from 0.0001 to 0.45 are quantified by calculating the normal force defect ξ and pitch damping factor ζ. Figure 4 summarizes the surface pressure results obtain for airfoil in terms of normal force defect and pitch damping factor [15]. Initially, increase in κ causes rise in ξ up to a certain limiting value where maximum normal force defect is attained ($\xi_{max} \approx 0.88$ for the band of $\kappa \approx 0.15$ to 0.20). Further rise in κ causes drop in the normal force defect. ξ_{max} defines the limiting condition for the reduced frequency up to which the maximum hysteresis is attained. For the given model configuration, in terms of varying κ, fully developed and partially developed dynamic stall regimes are identified.
Pitch damping factor initially shows negative damping ($\zeta < 0$) at lower κ ($\kappa < 0.02$). At $\zeta = 0$, the state of oscillatory motion and external flow are neutrally stable. Beyond $\kappa > 0.02$, $\zeta > 0$ and continuously shows rise in positive damping. Thus the energy is transferred from the oscillating airfoil to the external flow and no evidence of stall flutter is observed for $\kappa > 0.02$. Beyond the limiting condition, at $\kappa = 0.3$ (partially developed dynamic stall regime) ζ shows a sudden incremental positive jump. This indicates the severe impact of oscillation dynamics coupled with partially developed DSV which may lead to a certain flow phenomena to be critically assessed [15, 16, 17, 18, 19]. PIV Test obtained simultaneously along with the pressure measurement for specified test runs were processed and analyzed. As per the derived unsteady regimes, selected cases of κ are opted for further discussion.

The free-stream velocity measured upstream of the airfoil model is also subjected to unsteadiness induced due to motion dynamics of airfoil model oscillating at varying reduced frequency. These time-dependent free-stream velocity signals can be divided in two distinct parts viz. the mean-velocity component U_m (t) and the fluctuating-velocity component $u'(t)$. Figure 4(c) indicates the quantified unsteadiness due to the mean flow and fluctuating flow components at varied κ for Re = 0.2E06. The deviation in free-stream velocity is found be within 2.5% of the mean free-stream velocity for all the range of reduced frequencies tested. The general trend of unsteadiness established in this plot indicates that, at a constant Re with rise in κ, the unsteadiness of mean flow and fluctuating flow shows no significant changes up to a certain limiting value of κ = 0.038, beyond that mean flow shows reduction and the fluctuating flow shows rise in the unsteadiness of the time-dependent free-stream velocity. For the limiting fully developed dynamic stall regimes ($0.15 < \kappa < 0.20$) the unsteadiness induced due to mean-velocity component shows drastic reduction which continues to drop further for partially developed regime as well ($\kappa > 0.20$). The fluctuating-velocity components are found to be more dominant in these regimes as compared to the fully developed dynamic stall regime below the limiting ξ_{max} condition ($\kappa < 0.15$)

PIV and Surface Pressure Analysis:

Comparative pressure and PIV analysis are carried out for the following selected cases. PIV analyses are well supported by the time series C_P distribution and the sectional aerodynamic characteristics drawn from the integration of phase-averaged surface C_P distribution. Number of instantaneous frames of PIV images has been acquired for every oscillatory cycle of the motion. Certain instantaneous frames at varied angle of attack, covering a distance of $\approx 1.5c$ downstream from the TE, during the pitch-up and pitch-down motion are considered here for detailed analysis for the following cases.

Case-1; κ = 0.01, 0.10 ($\xi < \xi_{max}$): (Figures 5 to 7)
Figure 5 (a) & (b) represents the flow-field at pre-stall angles $\alpha = 12.23^o$ & 14.74^o for $\kappa = 0.01$. They show no sign for the inception of DSV during the pitch-up motion. The center of pressure is in the vicinity of quarter-chord line. Figure 5(b) indicates the C_n-surge point where flow reversal appears and the boundary layer begins to thicken at the rear portion of the airfoil followed by the moment stall. Center of pressure shows incremental jump and move downwards at the aft of quarter-chord line. Figure 5(c) at $\alpha = 17.08^o$ shows the growth of wake in the downstream TE vicinity because of the development of TEV. The primary LEV (DSV) moves on the upper surface of the airfoil model towards the TE followed by the lift stall where the DSV completely sheds-off the TE. Figure 5(d) at $\alpha = 19.09^o$ follows the lift stall where the large DSV is clearly visible downstream at the aft of TE enlarging the wake. It also triggers the movement of secondary vortex likes structure on the upper surface of the airfoil moving towards the TE. Further the progressive DSV and TEV completely leaves the airfoil TE and move downstream. Although potentially both DSV and TEV tend to move down the wake in the downstream region, the rotation sense of both DSV and TEV are opposite. DSV shows clockwise rotation and TEV shows anticlockwise rotation, both advances towards downstream to form large wake. Even secondary vortices which followed the DSV, completely sheds-off the TE at point 'e' as represented in figure 8.3(e) at $\alpha = 20.28^o$. The flow gets fully separated and at this location, the center of pressure gets paused ($X_{cp} \approx 0.38$) with no further incremental changes in its position. Fully separated flow in shown figure 5(f) at $\alpha = 23.62^o$ where the DSV and TEV collides and creates mushroom-like flow structure in the downstream wake region. The convective velocity of TEV seems to be lesser than the convective velocity of DSV. TEV also referred as starting vortex develops and progresses prior to the inception and growth of DSV. At an instant due to the differences in the strength and convective speed of DSV and TEV, causes the generation of mushroom-like flow structure. This structure gets perturbed further as the airfoil advances the maximum incidence at $\alpha = 24.78^o$ shown in figure 5(g). Figure 5(h) at $\alpha = 24.86^o$ indicates the start of pitch-down motion with large separated flows. As shown in figure 5(i) at $\alpha = 22.69^o$, the flow still continues to be fully separated. For figure 5(j) at $\alpha = 19.51^o$, the inception of secondary vortices occur and provide low order fluctuations on the upper surface of the airfoil model. Figure 5(k) at $\alpha = 15.29^o$ shows the initialization of the progressive reattachment process followed by the complete reattachment. Figure 5(*l*) at $\alpha = 10.15^o$ shows the complete attached flow with thin wake in the downstream. The entire chronology of dynamic stall events are well captured in figure 5(a-*l*). At the downstream of flow, the progressive motion within the wake is oscillatory in nature.

For higher reduced frequency within the fully developed dynamic stall regime at $\kappa = 0.10$, hysteresis loop being large and PIV images captured are well within this loop except of the first image which is in the pre-stall region. Figure 6(a) shows a completely attached flow during the pitch-up motion at $\alpha = 16.18^o$. C_n-surge, moment stall and lift stall do occur between points 'a' and 'b' of the figures 7, 9. Figure 6(b) at $\alpha = 23.8^o$ shows progression of DSV and TEV from TE towards the downstream wake. Further rise in the angle of attack at $\alpha = 24.1^o$ depicts some larger growth in wake as DSV and TEV separates away from each other as shown in figure 6(c). The airfoil reaches the maximum incidence and advances further for the pitch-down motion. Figures 6(d) & (e) shows the fully separated flows at $\alpha = 22.05^o$ & $\alpha = 21.9^o$ respectively. Further at point 'f' of figures 7, 9; the entrainment energy gets introduced from the upper free-stream flow to initiate the reattachment process. As a result, the wake size reduces which is shown in figure 6(f) at $\alpha = 12.44^o$. Further rise in pitch-down motion leads to the re-introduction of LSB, which collides with the secondary vortices from the upper surface, to track the transition path and to form complete reattached flow. Due to significant rise in hysteresis, comparative adverse changes are also observed in the center of pressure during the pitch-down motion prior to reattachment.

Case-2; κ = 0.15, 0.20 ($\xi \approx \xi_{max}$): (Figures 10 to 13)
Here in both the cases, hysteresis effect is in the limiting band of maximum (ξ_{max}) as shown in figure 4(a) & (b). There is also some incremental drop in the pitch damping factor among the two cases taken for analysis which suggest incremental shift in energy from fluid to the oscillating airfoil model. Figures 10(a) at $\alpha = 23.72^o$ for $\kappa = 0.15$ and 11(a) at $\alpha = 24.51^o$ for $\kappa = 0.20$, indicates the progression of DSV on the upper surface of the airfoil model, from LE towards TE triggered from the moment stall. In both cases, the model is just on the verge of reaching maximum angle of incidence and about to reach the lift stall point where DSV tends to shed from the TE. Here, for $\kappa = 0.15$ case, the convective velocity of the DSV seems to be marginally high than the oscillating speed of the airfoil model promoting the shedding of DSV from the TE as shown in figure 10(b) at $\alpha = 25^o$. Further DSV combines with the TEV to form progressive flow structures moving down the wake. The growth of these flow structures continues even during the pitch-down action of the airfoil model as seen is figure 10 (c) at $\alpha = 24.21^o$. The convection rate of entrainment energy from the free stream flow appeared to be less as compared to the pitch-down oscillation causing large delays in the promotion of reattachment process indicated by figures 10(d) & (e) at $\alpha = 20.92^o$ & 16.02^o respectively. And, by the time the reattachment process is just about to initiate as referred by point 'f ' and visualized in figure 10(f) at $\alpha = 9.79^o$, the airfoil model reaches the minimum angle of incidence with no reattachment occurring during the entire pitch-down motion. However as the reattachment process was already initiated, the energy still sustains to promote complete flow

reattachment just at the inception of pitch-up motion. But for $\kappa = 0.20$ case, as visualized from figure 11(b) at $\alpha = 25^o$, the convective velocity of DSV is marginally less than the oscillating speed of airfoil. Also from the same figure the growth rate of TEV is dominant as compared to the DSV. The airfoil reaches the maximum incidence, TEV roll-off on the upper surface from the TE and the DSV which was not fully developed then, is blocked by the TEV and gets trapped on the upper surface. This is also clearly visible in time series C_P distribution plot as shown in figure 12. Thus flow never gets fully separated for the entire pitch-up cycle. Further, the pitch-down motion initiates and the TEV weakens to allow the trapped under-developed DSV to partially shed out from the upper surface and promote full separation as seen in the instantaneous frames of figure 11(c), (d) & (e) at $\alpha = 23.73^o$, 23.43^o & 23.24^o respectively. Figure 11(f) at $\alpha = 14.82^o$ shows continuous rise in the entrainment energy with slower rate as compared to the pitch-down motion. This causes delay in the commencement of reattachment process and the flow gets reattach completely just at the inception point of pitch-up motion. Due to the marginal drop in the convective speed of DSV as compared to the pitch-rate of oscillating airfoil , the trapping of DSV on the upper surface and rise in the entrainment energy from the free-stream flow results in the incremental drop in the pitch damping factor for $\kappa = 0.20$ case. Similar adverse changes are also observed in the center of pressure during the pitch-down motion for the both the cases.

Both the cases up to greater extent retains the transition path traced by the LSB with minimum phase lag, gives rise to maximum hysteresis, limits the fully developed dynamic stall regime and initiates the partially developed dynamic stall regimes which are discussed in the next section.

Case-3; $\kappa = 0.30, 0.40$ ($\xi > \xi_{max}$): (Figures 14 to 17)
Figure 14(a) at $\alpha = 25^o$ for $\kappa = 0.40$ & figure 15(a) at $\alpha = 21.98^o$ for $\kappa = 0.40$ shows the movement of partially developed DSV on the upper surface with no trace of any development of TEV. But as the airfoil reached the maximum angle of attack, further movement of DSV on the upper surface gets stuck. Further the pitch down motion begins and TEV grows and roll-off on the upper surface to trap the progressing DSV. Instantaneous images of figure 14(b), (c) & (d) at $\alpha = 19.69^o$, 19.21^o & 19.1^o respectively for $\kappa = 0.30$ and figure 15(b) & (c) at $\alpha = 11.42^o$ & 11.24^o respectively for $\kappa = 0.40$, shows the collision of DSV and TEV on the upper surface, TEV weakens, DSV breaks up and flow gets separated. The separated flow still prevails as shown in figure 14(e) & (f) at $\alpha = 8.16^o$ & 7.62^o. They show no sign of reattachment during the entire pitch-down process. The process of reattachment initiates during pitch-up motion as shown in figures 15(d) & (e) at $\alpha = -1.7^o$ & -1.25^o respectively. Figure 15(f) at $\alpha = 4.83^o$ represents the completely attached flow. As shown in time series C_P distribution in figure 16, for the first time, the transition path traced by the LSB during the pitch-up and pitch-down got affected in this partially developed dynamic stall regimes. Even for $\kappa = 0.40$ case, no significant trace of LSB is detected. Thus the reduce frequencies beyond the limiting fully developed dynamic stall regime shows significant effect in weakening onset and reformation of LSB during the entire cycle of oscillation. The pitch-down cycle for both the case shows adverse changes in the center of pressure at a particular instant where a sudden jump from LE to TE is observed. This is due to the energy transfer from the oscillatory pitching down airfoil to the fluid causing incremental rise in pitching moment as well (nose-up).

CONCLUSION

PIV results demonstrates qualitative flow visualization of various dynamic stall chronology at varied reduced frequencies for a given *Re*. Distinct flow structures of DSV, TEV, mushroom-like flow structures, flow separation, flow reversal, wakes etc are clearly depicted for these PIV images. It helped in understanding the dynamic stall phenomena to greater extent along with the sectional aerodynamic characteristics derived from the surface pressure distribution measured simultaneously along with the PIV image capturing.

Reflection issues on the upper surface of airfoil due to laser light sheet persist to certain extent which fails to resolve the near-surface information more distinctly as compared to the surrounding flow-field.

Surface pressure and PIV helps in resolving the local and flow-field characteristics surrounding the oscillating airfoil but only limited to the mid-span (sectional domain) where the flow has closer resemblance to 2D configurations.

ACKNOWLEDGEMENT

We convey our sincere thanks to AR&DB (Aeronautical Research & Development Board), INDIA for funding the project and acknowledge the support for faculty members, Technical and administrative staff at the Department of Aerospace Engineering (IIT Kanpur) and National Wind Tunnel Facility (IIT Kanpur). The in time technical support provided from TSI Inc. USA is also appreciated.

REFERENCES

[1] Carr, L.W., McAlister, K.W. and McCroskey, W. J. (1977) "Analysis of the Development of Dynamic Stall based on Oscillating Airfoil Experiments." NASA TN D-8382.

[2] McCroskey, W J. (1981) "The Phenomenon of Dynamic Stall." NASA TM 81264.

[3] Shih, C., Lourenco, L., Van Dommelen, L., and Krothapalli, A. (1992) "Unsteady Flow Past an Airfoil Pitching at a Constant Rate." AIAA Journal, Vol. 30(5), pp. 1153-1161.

[4] Shih, C., Lourenco, L.M. and Krothapalli, A. (1995) "Investigation of Flow at Leading and Trailing Edges of Pitching-Up Airfoil." AIAA Journal, Vol. 33(8), pp. 1369-1376.

[5] Muti Lin, J.C. and Pauley, L. L. (1996) ".Low-Reynolds Number Separation on an Airfoil." AIAA Journal, Vol. 34(8), pp. 1570-1577.

[6] Lee, T. and Gerontakos, P. (2004) "Investigation of flow over an Oscillating Airfoil." Journal of Fluid Mechanics, Vol. 512, pp. 313-341.

[7]Abbott I.H. (1958) Theory of Wing Sections, Dover Publications, New York.

[8] Holm, R. and Gustavsson, J. (1999) "A PIV study of Separated Flow around a 2D Airfoil at High Angles of Attack in a Low Speed Wind Tunnel." FFA TN 1999-52.

[9] Berton, E., Favier, D., Maresca, C. and Benyahia, A. (2002) "Flow Field Visualizations around Oscillating Airfoils." LABM Laboratory, UMSR, Marseille, France.

[10] Tinar, E. and Cetiner, O. (2006) "Acceleration Data Correlated with PIV Images for Self-induced Vibrations of an Airfoil." Experiments in Fluids, Vol. 41(2), pp. 201-212.

[11]Ferreira, C.S. and Kuik, G. (2009) "Visualization by PIV of Dynamic Stall on a Vertical Axis Wind Turbine." Experiments in Fluids, Vol. 46, pp. 97-108.

[12]Adrian, R. J. (1991) "Particle-imaging techniques for experimental fluid-mechanics", Annual Review of Fluid Mechanics, Vol. 23, pp.261-304.

[13]Raffel, M., Willert, C.E, and Kompenhans, J. (1998) Particle Image Velocimetry - A Practical Guide, Springer, Berlin.

[14]Westerweel, J. (1997) "Fundamentals of Digital Particle Image Velocimetry." Measurement Science and Technology, Vol.8, pp.379-1392.

[15] Sharma, D.M. (2010) "Experimental Investigations of Dynamic Stall for an Oscillating Airfoil", PhD Thesis, IIT Kanpur

[16]Green, R.B. and Galbraith, R.A.McD. (1995) "Dynamic Recovery to Fully Attached Aerofoil Flow from Deep Stall." AIAA Journal, Vol. 33(8), pp. 1433-1440.

[17]Lee, T. and Basu, S. (1998) "Measurement of unsteady boundary layer developed on an oscillating airfoil using multiple hot-film sensors." Experiments in Fluids, pp. 108-117.

[18]Minniti III, R.J. and Mueller, T.J. (1998) "Experimental Investigation on Unsteady Aerodynamics and Aeroacoustics of a Thin Airfoil." AIAA Journal, Vol. 36(7), pp. 1149-1156.

[19]Kuo, C.H. and Hsieh, J.K. (2001) "Unsteady Flow Structure and Vorticity Convection over the Airfoil Oscillating at High Reduced Frequency." Experimental Thermal and Fluid Science, Vol. 24(3-4), pp. 117-129.

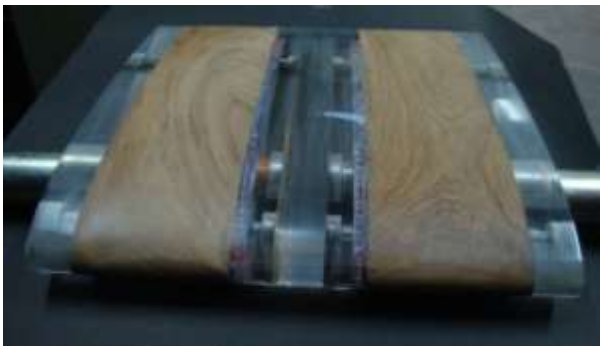

Figure 1 NACA0015 airfoil model for simultaneous Surface pressure and PIV measurements.

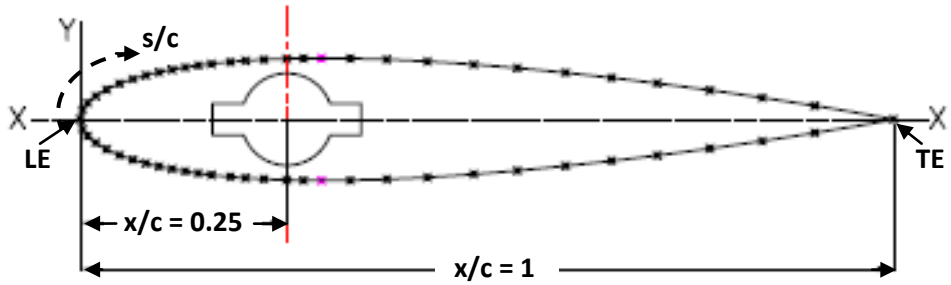

Figure 2 Pressure port locations opted for NACA0015 airfoil model

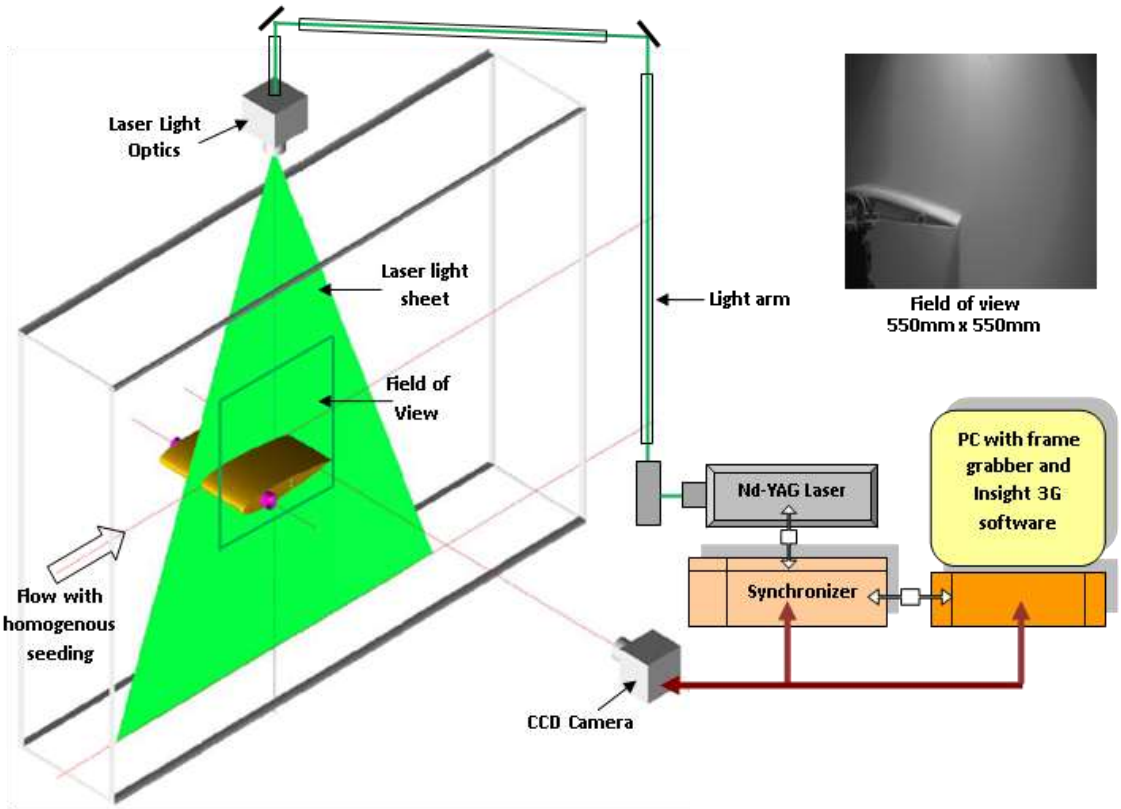

Figure 3 Measurement and Instrumentation chain for 2D-PIV measurement

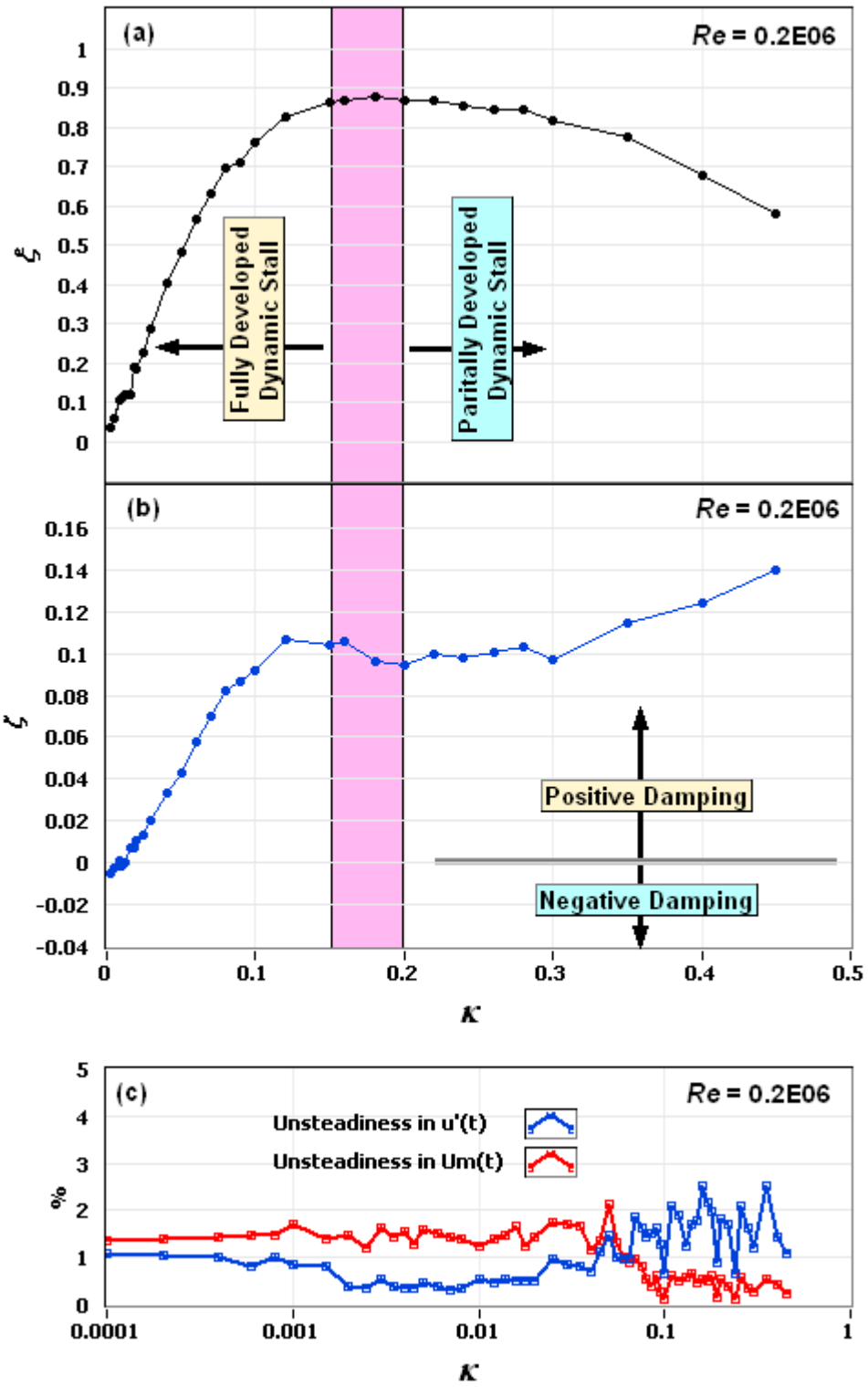

Figure 4 (a) ξ *vs* κ **(b)** ζ *vs* κ **(c)** Unsteadiness in U_∞ (%) *vs* κ**;** at *Re* = 0.2E06

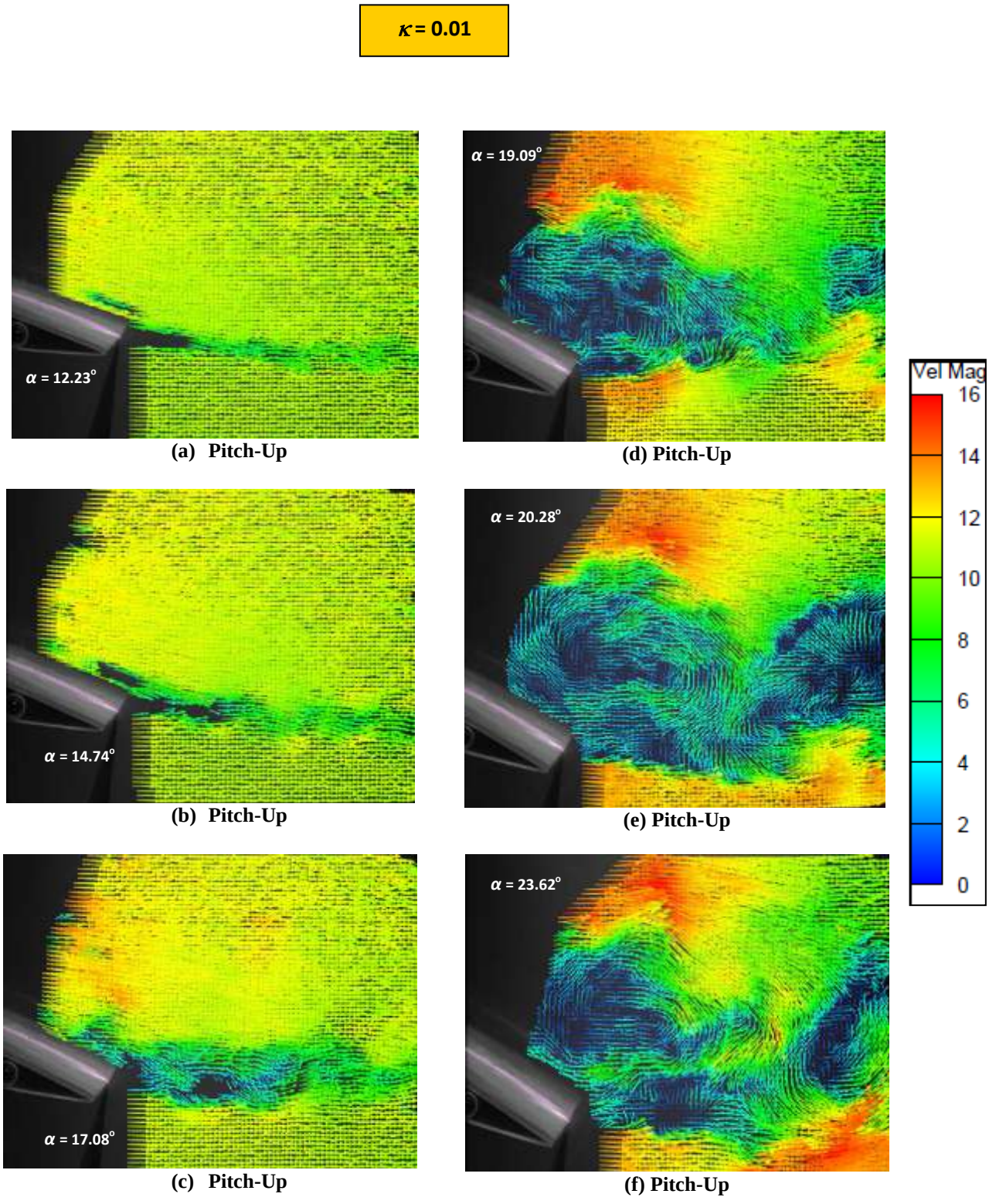

Figure 5 (a-f) PIV images at instantaneous angle of attack for $\kappa = 0.01$ at Re = 0.2E06

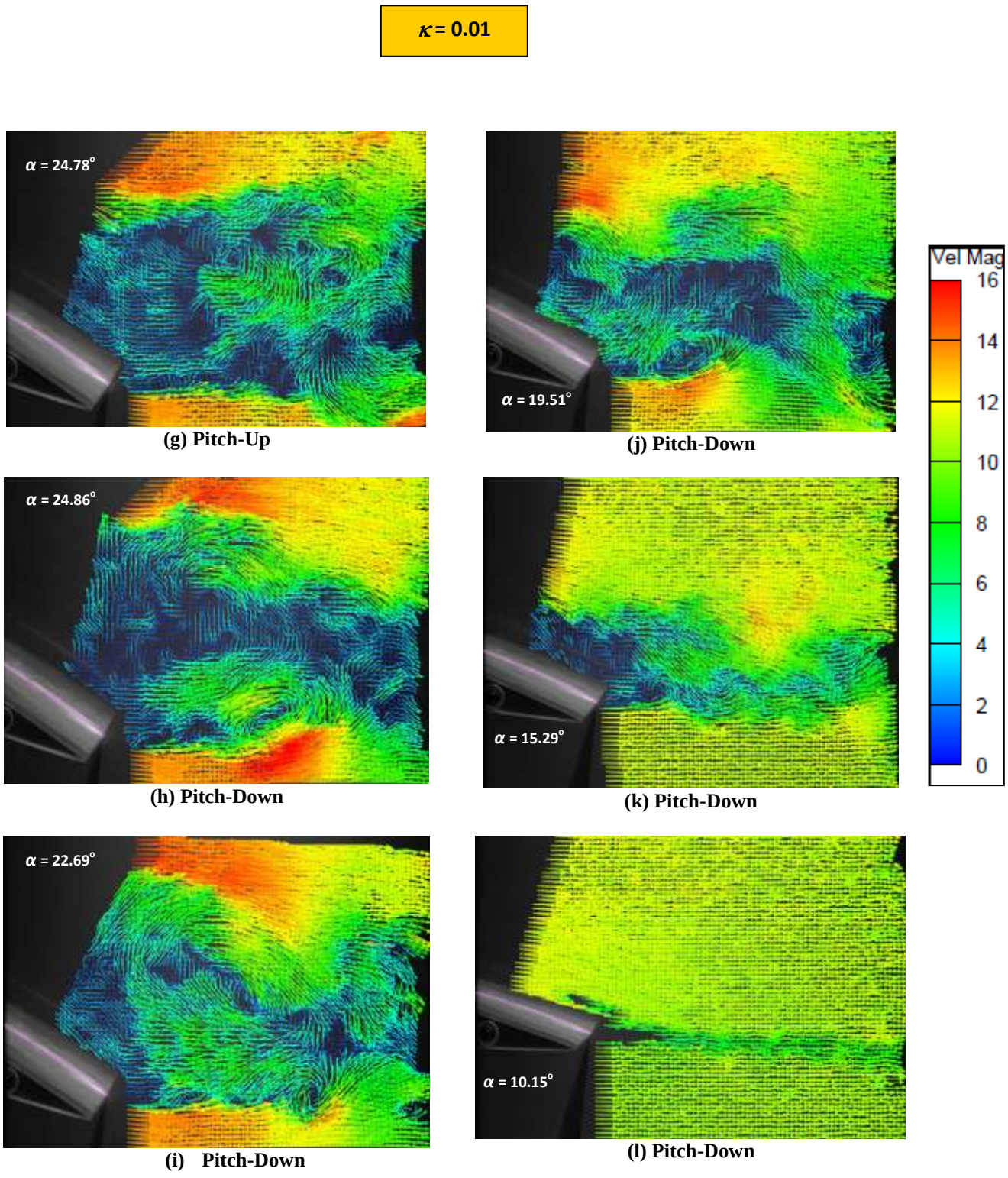

Figure 5 (g-l) PIV images at instantaneous angle of attack for $\kappa = 0.01$ at Re = 0.2E06

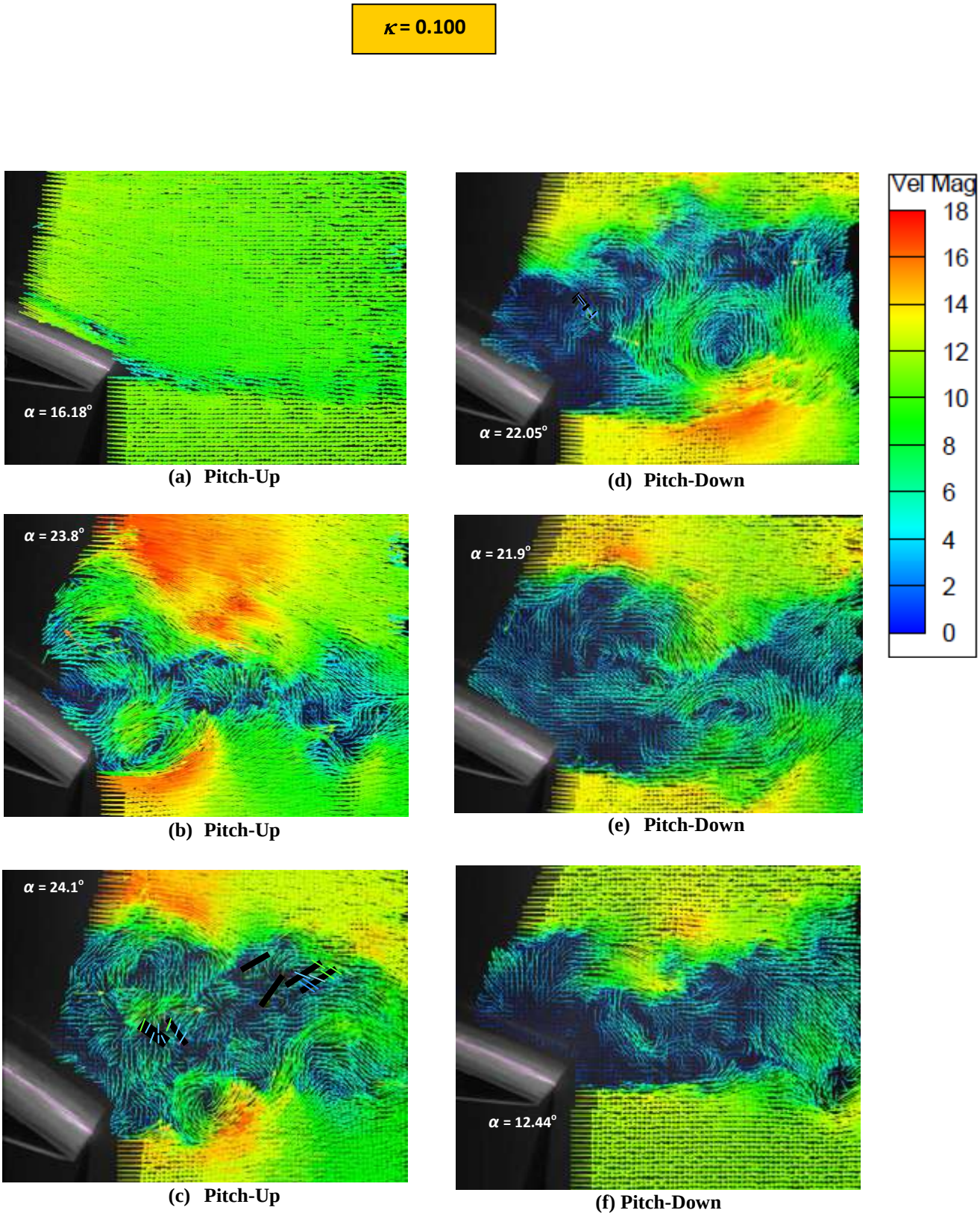

Figure 6 (a-f) PIV images at instantaneous angle of attack for $\kappa = 0.10$ at Re = 0.2E06

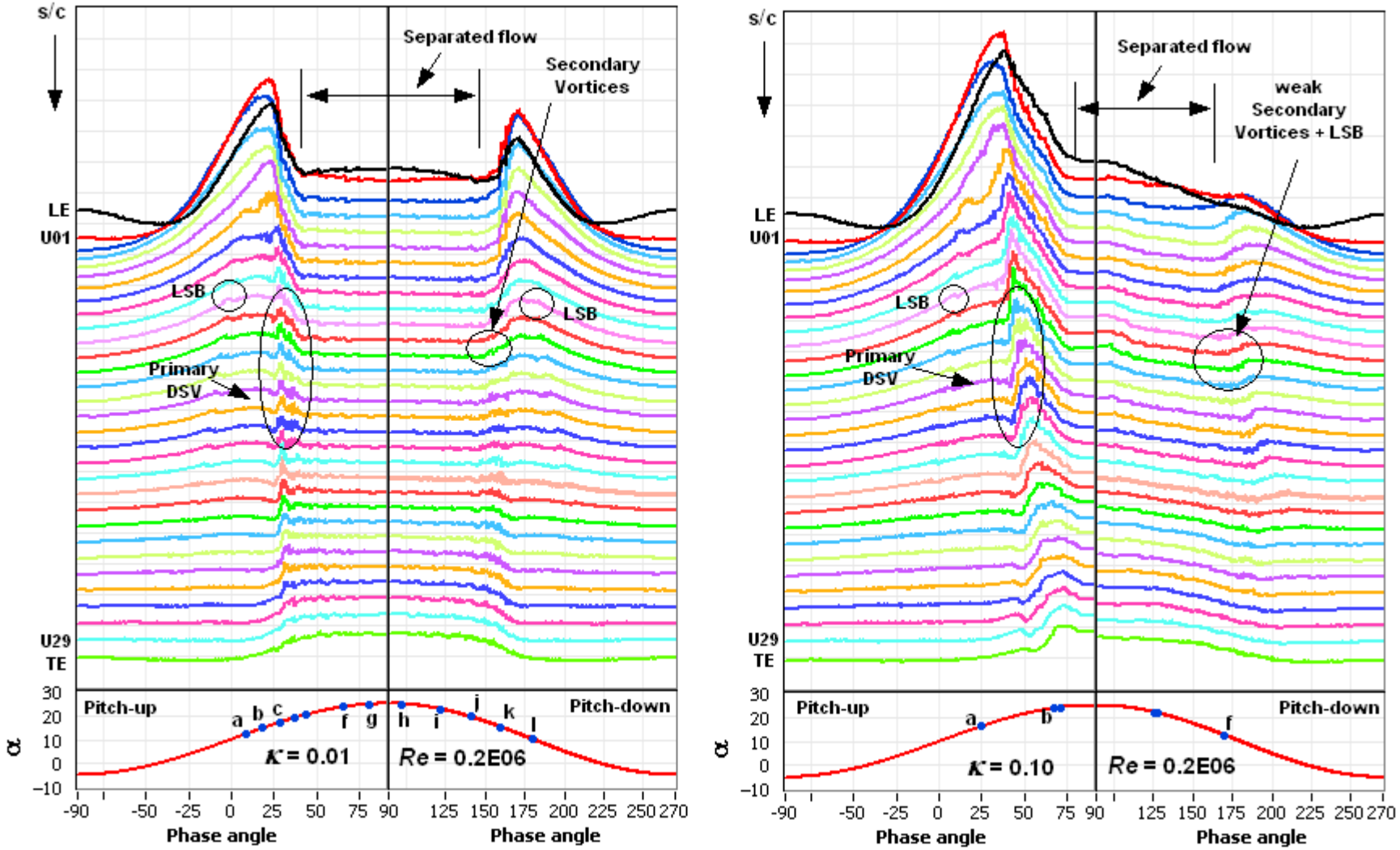

Figure 7 Time series C_p distribution for $\kappa = 0.01, 0.10$ at $Re = 0.2E06$

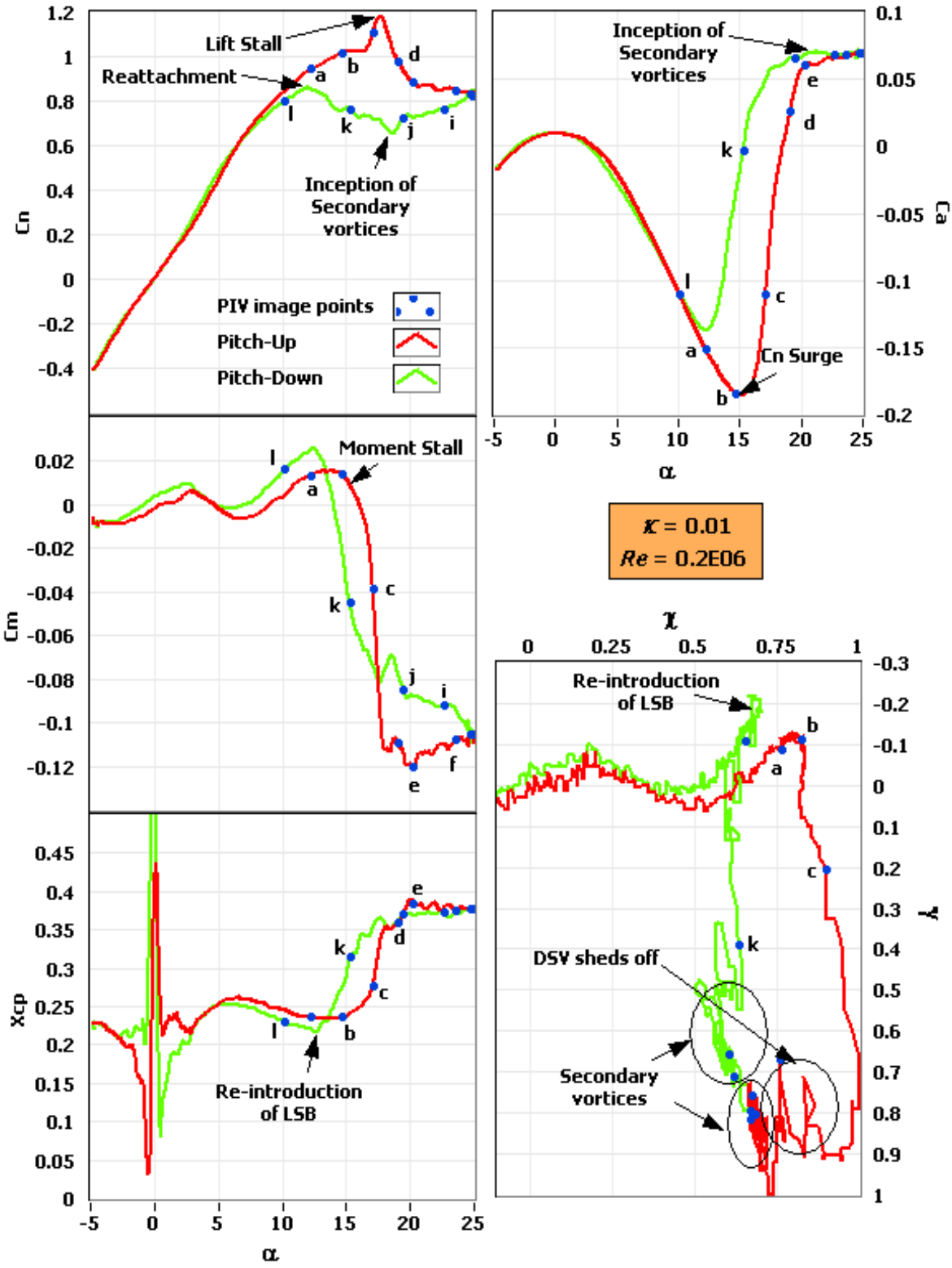

Figure 8 C_n *vs* α, C_m *vs* α, X_{cp} *vs* α, C_a *vs* α, χ-γ cross plot;
for Re = 0.2E06 at κ = 0.01

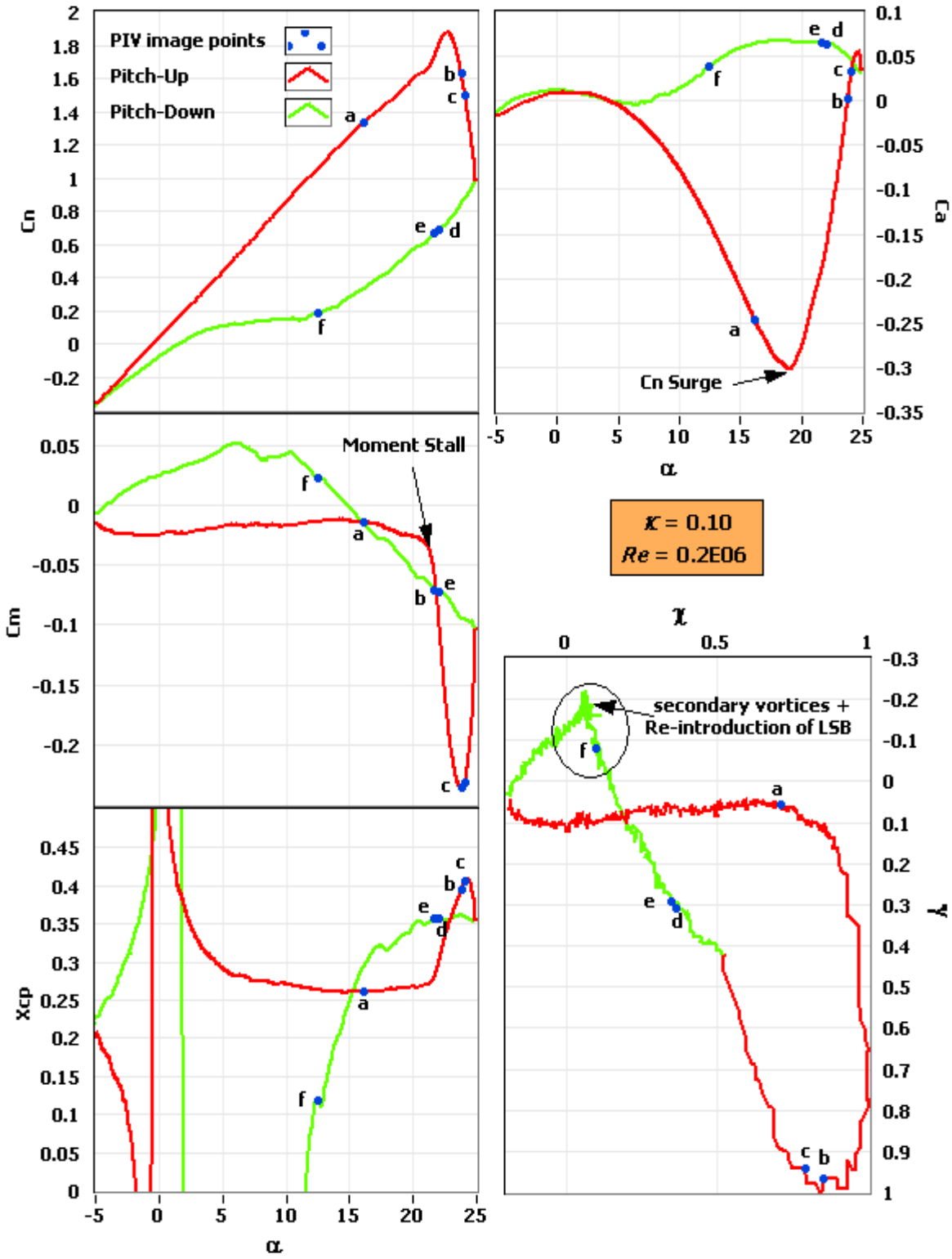

Figure 9 C_n *vs* α, C_m *vs* α, X_{cp} *vs* α, C_a *vs* α, χ-γ cross plot;
for Re = 0.2E06 at κ = 0.10

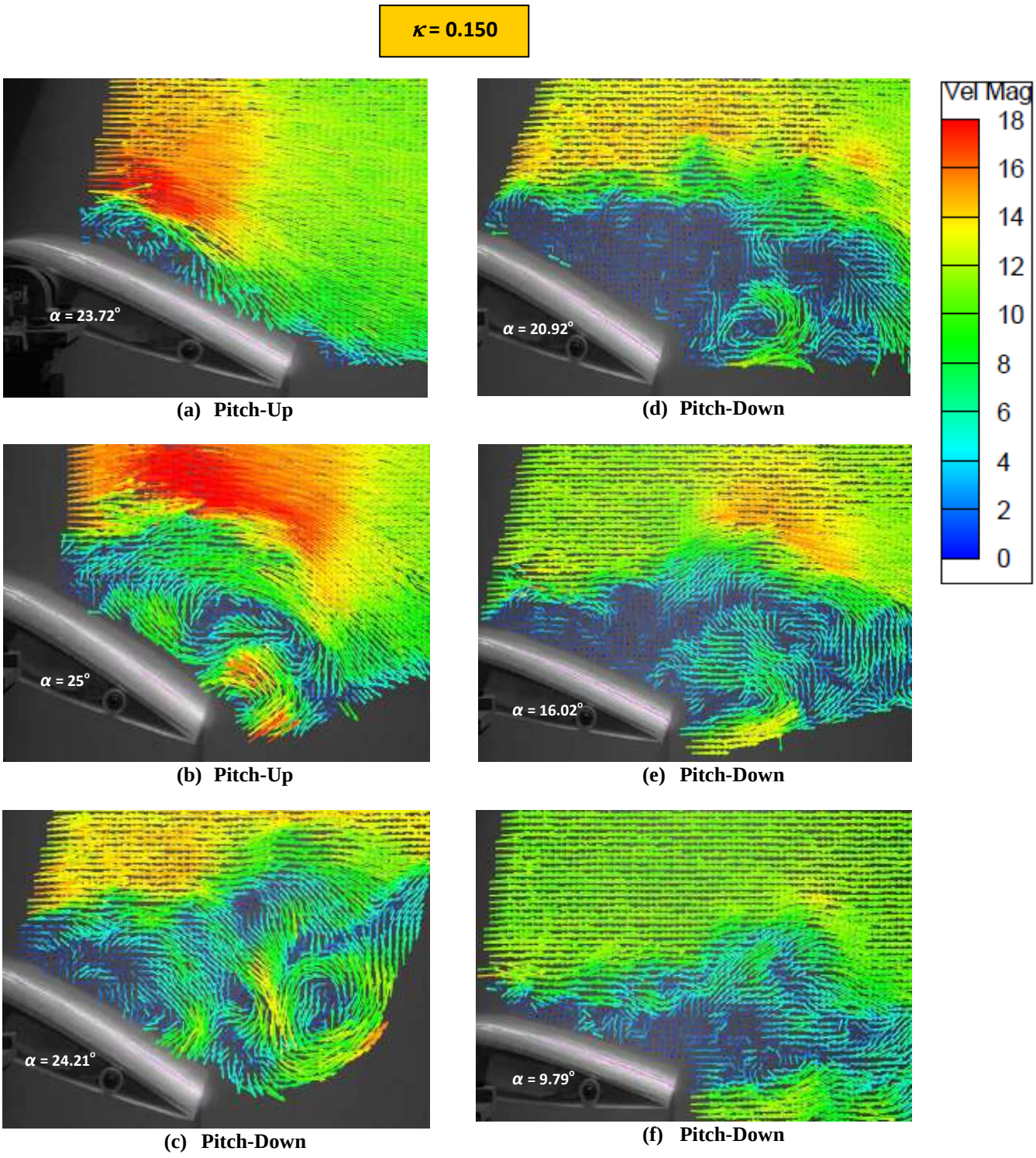

(a) Pitch-Up **(d) Pitch-Down**

(b) Pitch-Up **(e) Pitch-Down**

(c) Pitch-Down **(f) Pitch-Down**

Figure 10 (a-f) PIV images at instantaneous angle of attack for κ = 0.15 at *Re* = 0.2E06

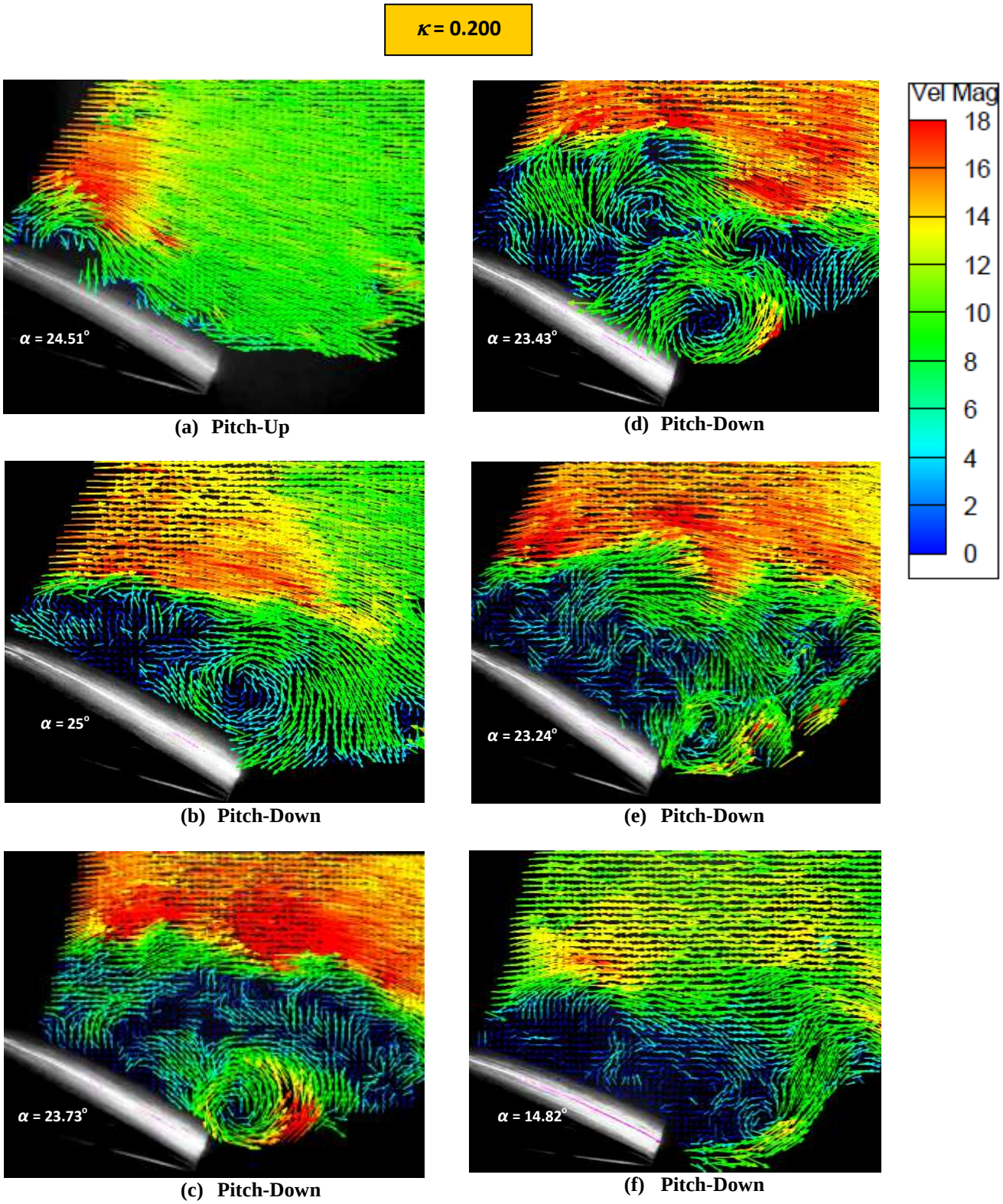

Figure 11 (a-f) PIV images at instantaneous angle of attack for κ = 0.20 at *Re* =

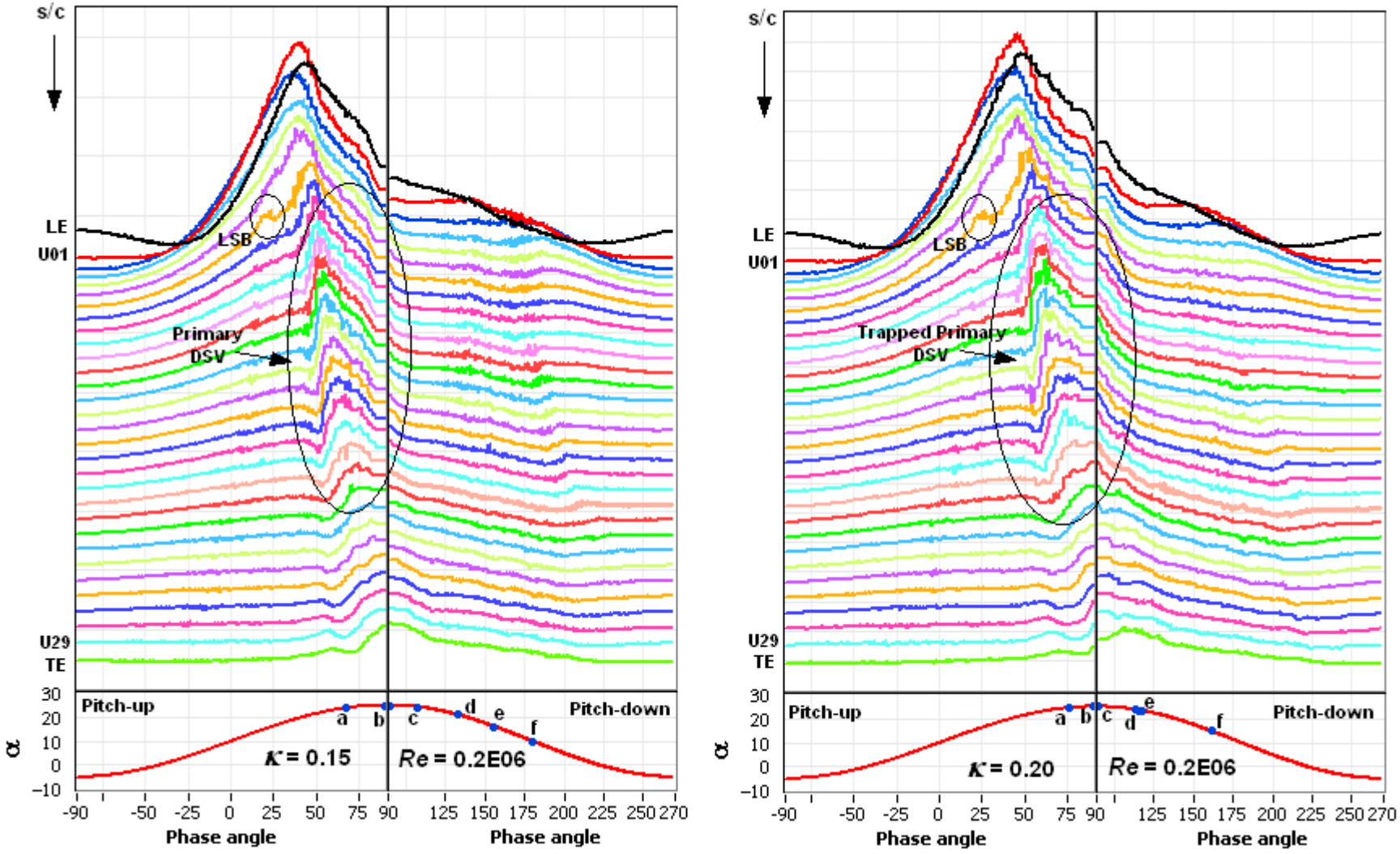

Figure 12 Time series C_p distribution for κ = 0.15, 0.20 at *Re* = 0.2E06

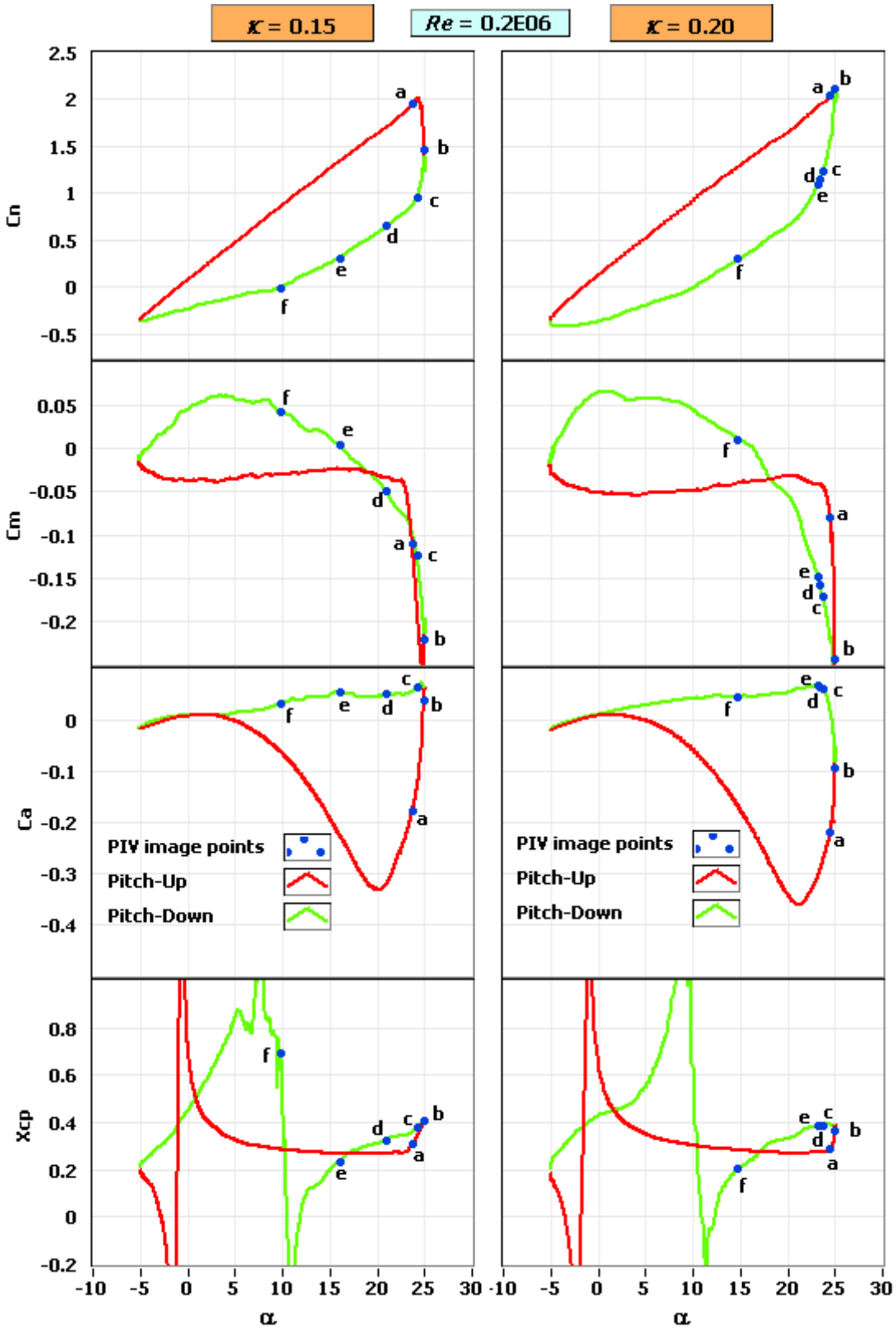

Figure 13 C_n *vs* α, C_m *vs* α, C_a *vs* α, X_{cp} *vs* α; for Re = 0.2E06 at κ = 0.15 & 0.20

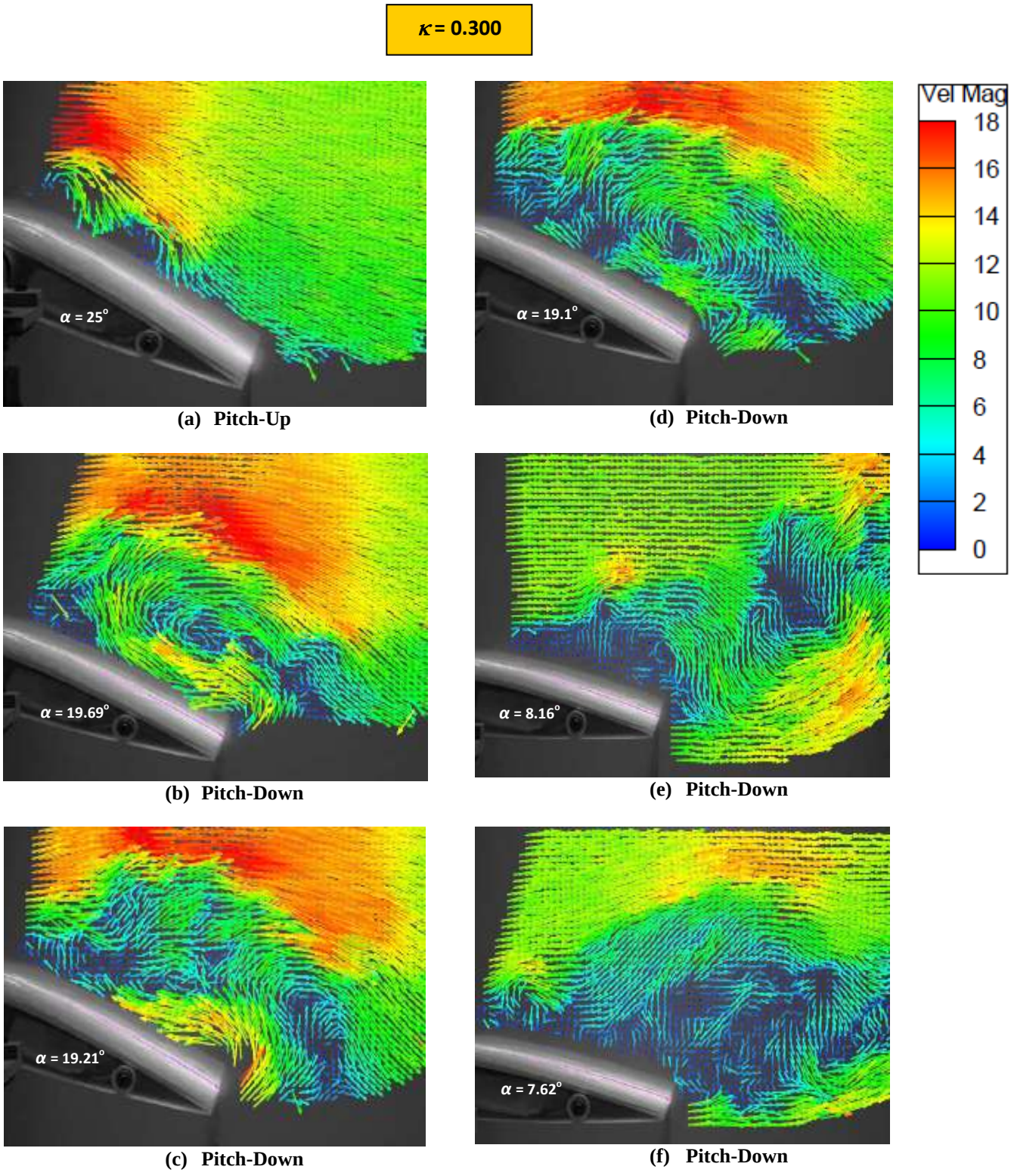

Figure 14 (a-f) PIV images at instantaneous angle of attack for κ = 0.30 at *Re* = 0.2E06

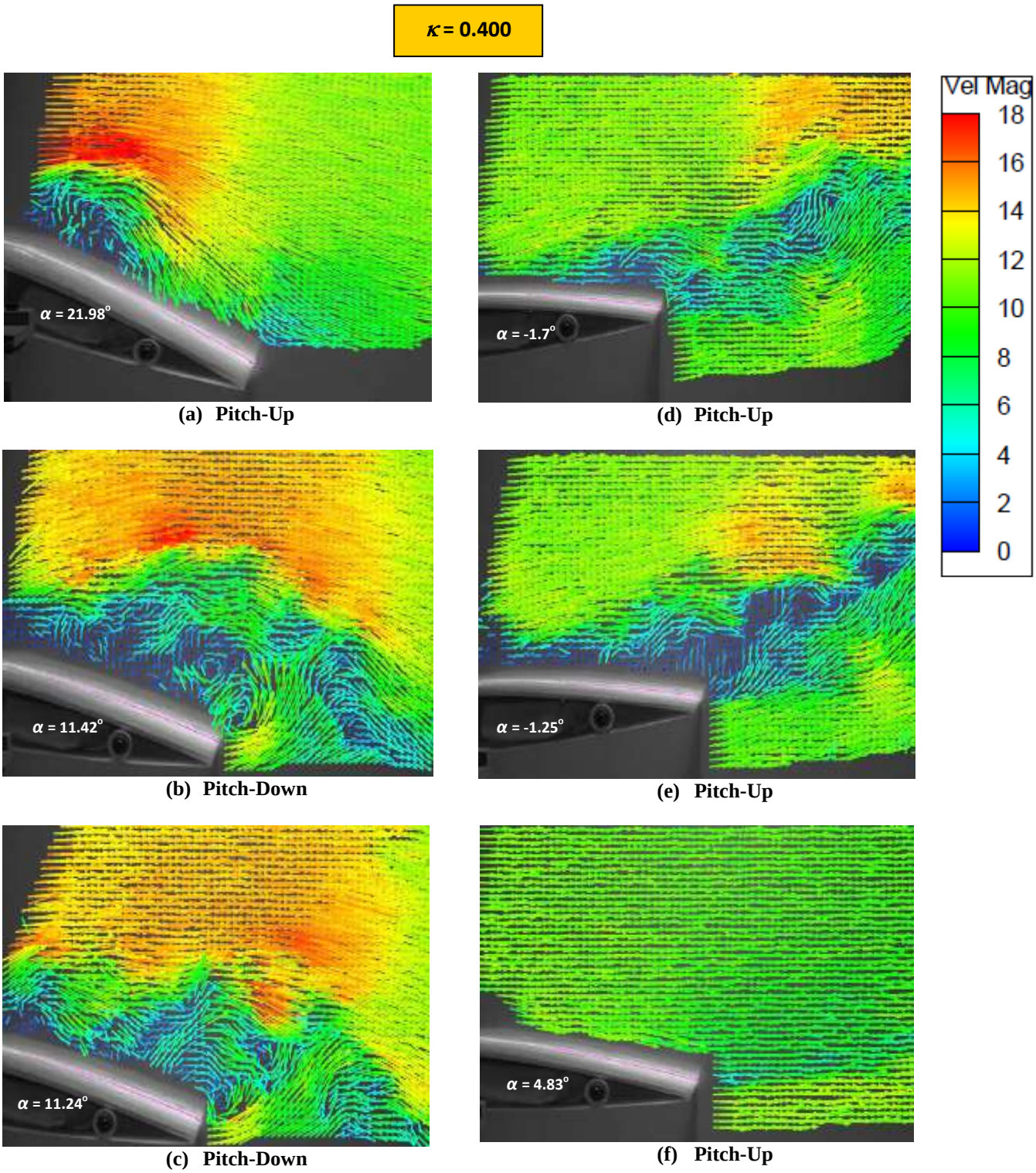

Figure 15 (a-f) PIV images at instantaneous angle of attack for κ = 0.40 at *Re* = 0.2E06

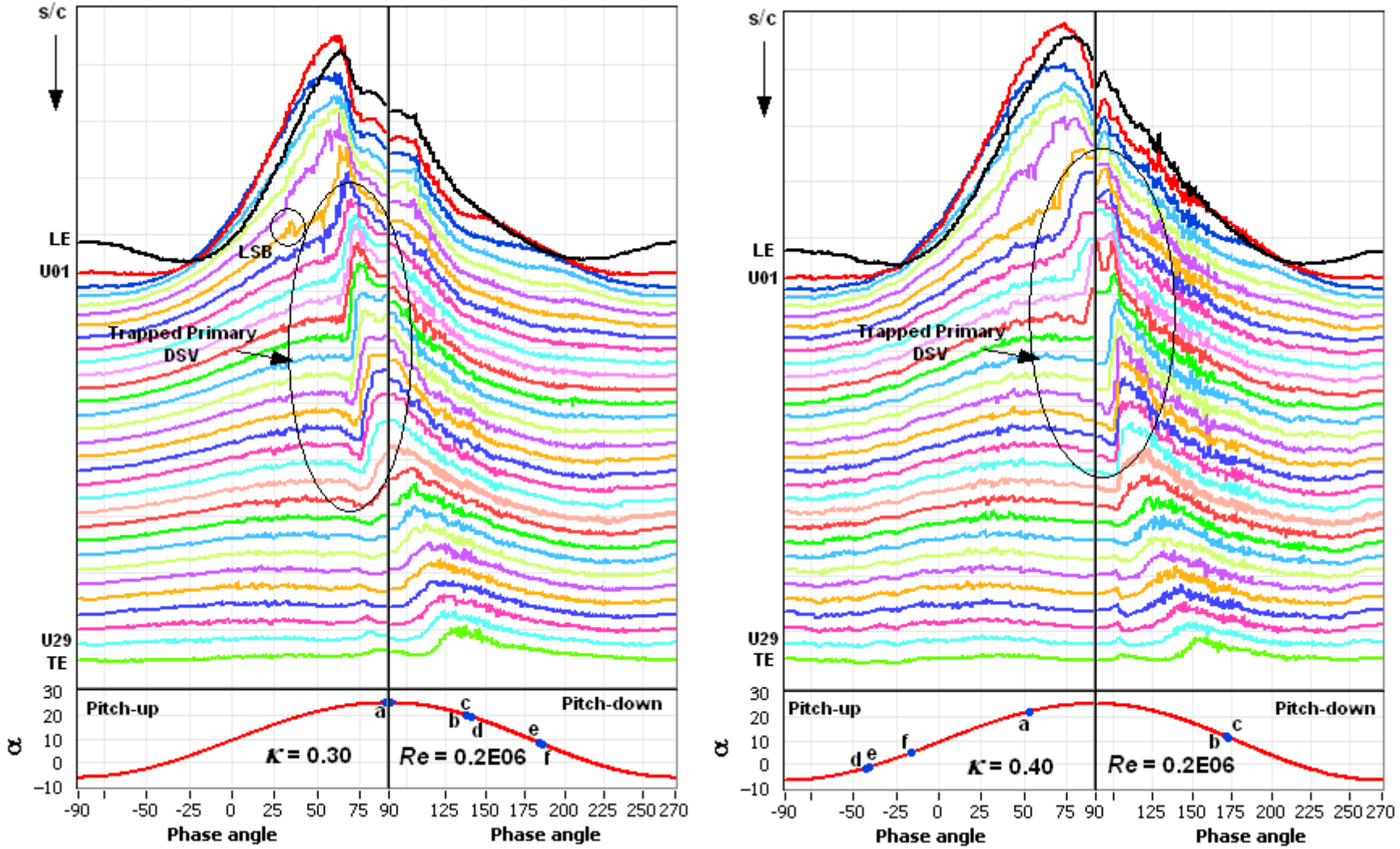

Figure 16 Time series C_P distribution for κ = 0.30, 0.40 at *Re* = 0.2E06

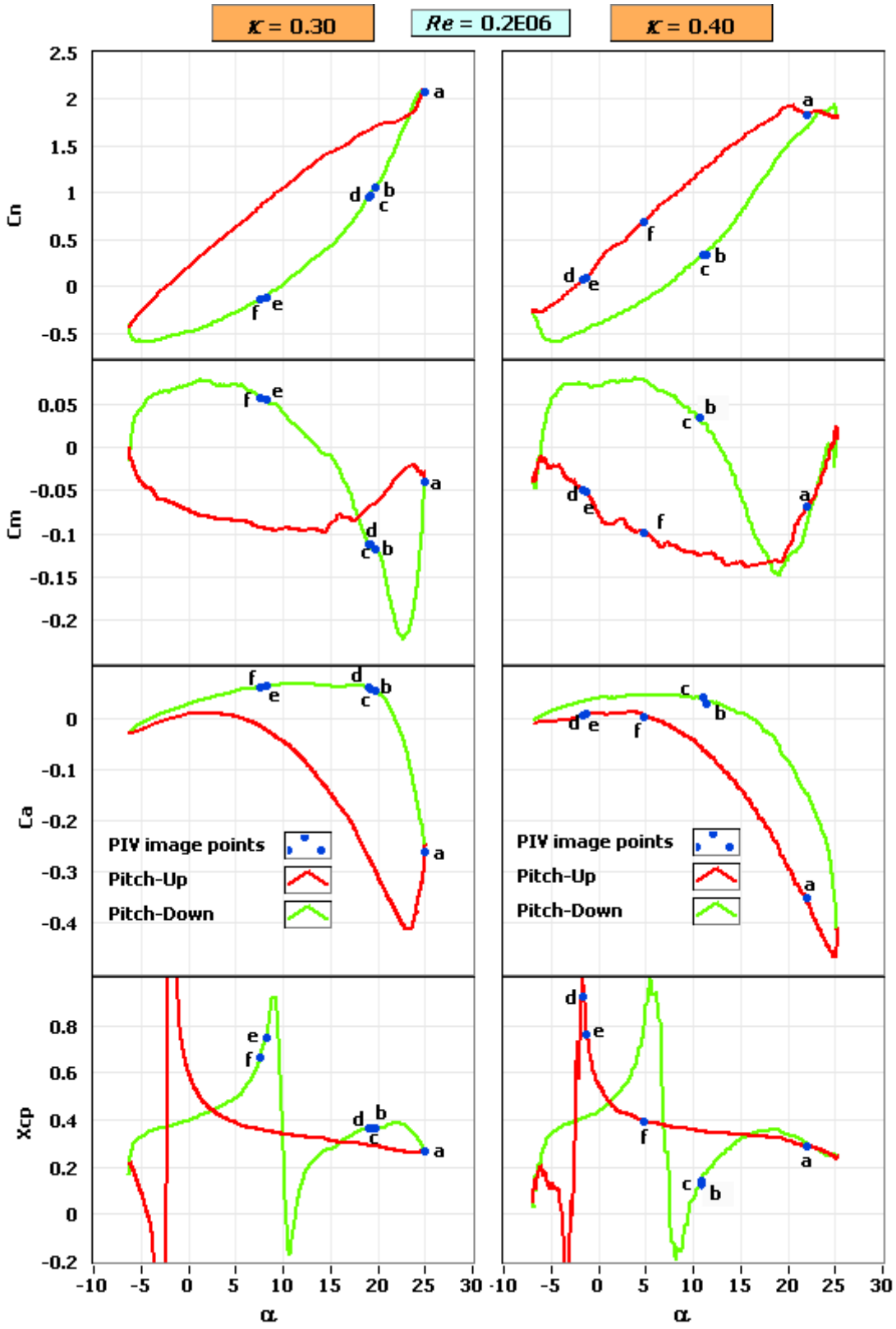

Figure 17 C_n *vs* α, C_m *vs* α, C_a *vs* α, X_{cp} *vs* α; for Re = 0.2E06 at κ = 0.30 & 0.40